

RESEARCH ARTICLE

Influence of optical clearing agents on the scattering properties of human nail bed and blood microrheological properties: In vivo and in vitro study

P. A. Moldon¹ | P. B. Ermolinskiy¹  | A. E. Lugovtsov¹  |
P. A. Timoshina^{2,3,4}  | E. N. Lazareva^{2,3,4} | Yu. I. Surkov^{2,3,4} |
Y. I. Gurfinkel⁵  | V. V. Tuchin^{2,3,4}  | A. V. Priezzhev¹ 

¹Department of Physics, Lomonosov Moscow State University, Moscow, Russia

²Institution of Physics, Saratov State University, Saratov, Russia

³Laboratory of Laser Molecular Imaging and Machine Learning, Tomsk State University, Tomsk, Russia

⁴Laboratory of Biomedical Photoacoustic, Saratov State University, Saratov, Russia

⁵Medical Research and Education Center, Lomonosov Moscow State University, Moscow, Russia

Correspondence

P. B. Ermolinskiy, Department of Physics, Lomonosov Moscow State University, 1-2 Leninskie Gory, Moscow 119991, Russia.
Email: ermolinskiy.pb15@physics.msu.ru

Funding information

Russian Science Foundation, Grant/Award Number: 23-45-00027; Ministry of Science and Higher Education of Russian Federation, Grant/Award Number: FSRR-2023-0007

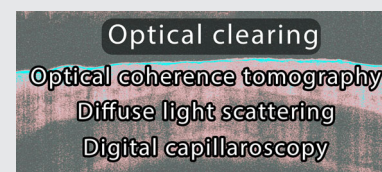
Abstract

Optical clearing agents (OCAs) are substances that temporarily modify tissue's optical properties, enabling better imaging and light penetration. This study aimed to assess the impact of OCAs on the nail bed

and blood using in vivo and in vitro optical methods. In the in vivo part, OCAs were applied to the nail bed, and optical coherence tomography and optical digital capillaroscopy were used to evaluate their effects on optical clearing and capillary blood flow, respectively. In the in vitro part, the collected blood samples were incubated with the OCA and blood aggregation properties were estimated using diffuse light scattering techniques. The results indicate that OCAs significantly influence the optical properties of the nail bed and blood microrheology. These findings suggest that OCAs hold promise for improving optical imaging and diagnostics, particularly for nail bed applications, and can modify blood microrheology.

KEYWORDS

digital capillaroscopy, nail bed, optical clearing agent, optical coherence tomography, RBC aggregation, RBC deformation, red blood cell



1 | INTRODUCTION

Over the past 20 years, optical technologies have demonstrated rapid and productive development; optical methods of diagnosis, monitoring and treatment have become widely used in medicine and cosmetology. Optical methods provide safe and noninvasive monitoring of

biological tissues, liquids, and show highly informative diagnostic potential. However, further development of optical technologies is often limited by the high scattering of light in biological tissues and fluids. Strong light scattering is due to the inhomogeneous structure of the objects under study, which includes components with different refractive indices. Optical clearing helps to solve the problem of high light scattering in biological tissues [1] and liquids [2], which limits the use of optical methods in biomedical optics due to the low light penetration depth [3–5]. Optical clearing is actively used to

study the microvascular system [6, 7], blood [8–10], various tissues [11–13] and their structural changes under the development of various pathologies [14, 15] and under the influence of external factors. Typically, optical clearing agents (OCAs) are applied to the surface of tissues, specifically on the skin of the brain and nail bed area. These areas of the skin, where the agents are applied, have a dense network of capillaries. OCA are osmotically active substances, and they can penetrate into the tissue and capillaries. Basically, that allows to locally modify the parameters of the light scattering [16]. Subsequently, one can expect an alteration of intrinsic mechanical properties of blood cells effecting their interaction with each other. The latter may significantly distort the results of the diagnostics. Because optical clearing is used not only for in vitro visualization but is also actively used and developed in diagnostics and therapy in vivo, it is necessary to study the mechanism of the influence of various OCA on biological tissue, blood vessels, organs, and the microrheological properties of blood, that is, red blood cell (RBC) aggregation and deformation [17]. Despite numerous works by various scientific groups, the question of the influence of OCA remains open and relevant [18–20]. In this work, to evaluate the effects of OCA in vivo we used digital capillaroscopy imaging of nail bed of healthy donors to assess possible changes in the hemodynamics and additionally characterize how usage of OCA can improve the quality of the capillaries imaging. In our in vitro experiments, we assessed the effects of several OCA on the microrheological parameters of blood. The combination of results obtained in vivo and in vitro allowed us to the characterize in detail the possible manifestations of some of the studied OCA in changes of blood microrheology and corresponding blood flow velocity in the microcirculation system.

2 | MATERIALS AND METHODS

2.1 | Optical clearing agents

In our studies, 98.2% glycerol solution, 50% glycerol-propylene glycol (PG) solution, polyethylene glycol (PEG) 300, cedar oil, oleic acid, 50% aqueous fructose solution, X-ray contrast agent Omnipaque-300[®], 60% solution Omnipaque-300-PG, X-ray contrast agent Visipaque-270[®] were used as OCAs.

These agents or their components separately are actively used in various works. For example, in the work [21], the effect of glycerol and Omnipaque-300[®] solutions on autofluorescence under two-photon excitation and background fluorescence under Raman at

different skin depths was studied. It is shown that Omnipaque-300[®] is a promising OCA due to its ability to reduce background fluorescence in the upper layers of the skin. Also, in the work [22], the interaction of the Omnipaque-300[®] and glycerol with collagen peptide mimetic (GPH)₃ as one of the main components of biological tissues was studied using classical molecular dynamics methods (GROMACS). Omnipaque-300[®] demonstrated lower optical clearing efficiency compared to glycerol, but Omnipaque-300[®] is a promising immersion agent that provides significant optical clearing of the skin without noticeable effect on tissue structure [22].

The efficiency of fructose application for the optical clearing as well as molecular interaction analysis was presented in the paper [23]. Similar modeling methods were used to study the effectiveness of glycerol in the work [24], where the authors considered different concentrations of aqueous glycerol solutions. The paper presents the results of molecular interaction studies of different PEGs [25]. In the paper [26], the authors showed using different spectral methods that PEGs can be used for optical clearing. In the work [3], the validation of Visipaque-270[®] as an OCA on the skin of laboratory mice using OCT, spectral and fluorescence imaging methods was carried out.

The refractive indices of solutions were measured at wavelengths 589 and 930 nm on the Abbe DR-M2/150 multi-wavelength refractometer (Atago, Japan). Table 1 shows the refractive indices of these solutions.

2.2 | Optical coherence tomography

For the OCT study, different OCAs were applied to the surface of the nail bed skin areas, that is, the nail fold area 2 mm from the eponychium, of six healthy volunteers. For each finger, only one OCA was used. Before the experiments, all fingers were washed with the ordinary soap. Each OCA was applied on the nail bed skin using a pipette, measurements were performed before applying the used OCA to the intact area, immediately after application of the OCA, then every 5 min for 15 min. Due to the fact that in this work the effectiveness of OCAs was assessed to analyze the possibility of their use in capillaroscopy, the main purpose of the study was to study short-term effects on the skin. According to various sources, after this period of time, the effect of optical clearing can either remain constant or decrease [33]. After each measurement, a tissue applicator moistened with OCA was placed on the area of interest to prevent drying. Before recording optical coherence tomography (OCT) images, residual liquids were carefully removed with a sterile cloth using blotting movements without

TABLE 1 Refractive indices of OCAs at wavelengths 589 and 930 nm.

#	OCA	MANUFACTURER	REFRACTIVE INDEX	
			589 nm	930 nm
1	98.2% glycerol solution (molecular structure in [27])	Reachem, Russia	1.4714	1.4647
2	50% glycerol-PG solution (molecular structure in [28])	Reachem, Russia; TLJT, China	1.4503	1.4422
3	Omnipaque-300 [®] (molecular structure in [29])	GE Healthcare, USA	1.4402	1.4298
4	60% solution Omnipaque-300-PG (molecular structure in [30])	GE Healthcare, USA; TLJT, China	1.4451	1.4356
5	Visipaque-270 [®] (molecular structure in [31])	GE Healthcare, USA	1.4245	1.4137
6	50% aqueous fructose solution (molecular structure in [27])	Sigma-Aldrich, USA	1.4310	1.4232
7	Cedar oil (molecular structure in [30])	AltaiBio, Russia	1.5160	1.4920
8	PEG-300 (molecular structure in [27])	Zavod sintalov LLC, Russia	1.4631	1.4560
9	Oleic acid (molecular structure in [32])	Radiacid, Belgium	1.4585	1.4509

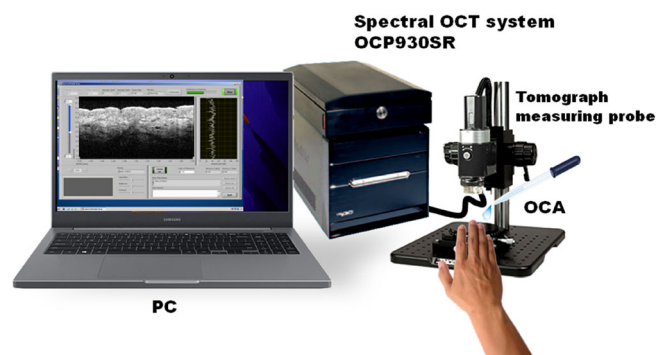


FIGURE 1 Experimental setup of the optical coherence tomography.

pressing. Immediately after OCT imaging, the OCA was reapplied to the area of interest.

Optical clearing of the nail bed was monitored using the commercially available spectral OCT system OCP930SR (Thorlabs, Newton, NJ) operating at a central wavelength of 930 ± 5 nm with a full width at half maximum of 100 ± 5 nm spectrum, numerical aperture 0.22, optical power 2 mW, maximum scanning depth 1.6 mm, scanning area length 6 mm. The axial and lateral resolutions were 6.2 and 9.6 μm , respectively. The experimental setup is shown in Figure 1.

The intensity of the OCT signal depends on the diffuse reflectivity of the biotissue at a given depth, determined by the local refractive index and local ability of the biotissue to scatter light. According to the single scattering model, the reflected light power is proportional to exponential expression (Equation 1):

$$R(z) = A \exp(-\mu_t z) + B, \quad (1)$$

where $R(z)$ is the reflected light power; μ_t is the attenuation coefficient; z is the depth; A is the optical power in the beam incident on the biotissue surface; B is the background signal.

In this work, the attenuation coefficient was assessed before exposure and during the application of OCAs. The maximum imaging depth was around 800 μm with pixel size—3 μm . Obtained 16-bit 2D scan images were processed with a Mathcad 14 program that calculated the value of the attenuation coefficient averaged over the region of interest. A detailed description of data processing is presented in the work [34]. From each image at different areas 5 values of the attenuation coefficient were calculated. The average values were normalized for the attenuation coefficient that was calculated from the images of the nail bed area before the application of OCA. By comparing the normalized attenuation coefficients one can conclude on the efficiency of specific OCAs for this tissue and wavelength.

Also, as a second method for assessing the effect of OCA on the optical properties nail bed skin the method of reconstructing the attenuation coefficient of the OCT signal with depth resolution was used. At each time point, five OCT images were recorded for three areas spaced no more than 500 μm from each other. OCT B-scans were obtained using spectral OCT GAN930V2-BU (Thorlabs, USA), operating at a central wavelength of 930 nm with axial and lateral resolution of 5.34 μm (in air) and 7.32 μm , respectively. The B-scan is a two-dimensional cross-sectional image showing the optical reflectance of structural elements of biotissue. A single B-scan is created by taking a series of A-scans (axial reflectance profiles) along a linear path on the tissue

surface. Each A-scan corresponds to a vertical “slice” of the tissue, and when they are placed side by side, they form a two-dimensional B-scan image. Variations in reflectance at different tissue depths result in image contrasts that allow differentiation of tissue layers and detection of structural abnormalities. The width of the OCT scanning window was 6 mm, the depth was 2.7 mm.

To analyze each OCT image, regions of interest (ROIs) free of OCT artifacts were identified by researchers experienced in interpreting OCT images and having published on the topic of OCT images. ROIs on OCT images were selected that were free of artifacts such as defocus artifacts, motion artifacts that could blur the structural image, specular reflection artifacts, and shadow effects in which the reflection of light from dense structures could blur the underlying tissue and its renderings are darker compared to adjacent identical biological tissues. The width of such ROIs varied from 3 to 5 mm; the height of the ROI was limited by the depth of OCT probing. For each pixel from the ROI, the attenuation coefficient of the OCT signal, μ_{OCT} , was calculated. To restore the attenuation coefficient of the OCT signal as a function of depth— $\mu_{\text{OCT}}(z)$, we used the algorithm proposed in [35]. This method is based on the single scattering model and two assumptions: (i) Almost all radiation is attenuated within the OCT probing depth range; (ii) the backscattered light that is recorded by the OCT system constitutes a fixed fraction of the attenuated probe radiation. In other words, it is assumed that the fraction of light backscattered from irradiated tissue and collected by the OCT system remains proportional to the attenuated light at the probing depth. These assumptions allow the attenuation coefficients to be estimated for each pixel in the data set without the need for a reference layer. Multiple scattered light is not taken into account, because the estimation of attenuation coefficients of different biotissues based on OCT measurements can be performed with sufficient accuracy using models based on single scattering if the biotissue sample has relatively low scattering and absorption coefficients ($<10 \text{ mm}^{-1}$) [36, 37]. According to this approach, the attenuation coefficient— $\mu_{\text{OCT}}(z)$, is determined by the Equation 2:

$$\mu_{\text{OCT}}(z) = \frac{I(z)}{\int_z^D I(u) du}, \quad (2)$$

where D is the scanning depth range of the OCT system, $I(z)$ and $I(u)$ are the intensity of the OCT signal at depth z and u , respectively.

Taking into account the discreteness of the OCT signal, Equation 2 takes the form:

$$\mu_{\text{OCT}}(i) = \frac{1}{2\Delta} \log \left(1 + \frac{I(i)}{\sum_{i+1}^N I(i)} \right), \quad (3)$$

where Δ is the pixel size, $I(i)$ is the intensity of the i th pixel, N is the number of pixels in the axial direction.

Equation 3 was used to calculate the attenuation coefficient of each pixel for all A-scans from the ROI. Reconstructed OCT signal attenuation coefficients were averaged laterally within the ROI for each OCT image. Due to the unevenness of the skin surface, before averaging the attenuation coefficient profile $\mu_{\text{OCT}}(z)$, an algorithm developed in MATLAB (The MathWorks, USA) was used for the calculation of the attenuation coefficient of the biological tissue surface.

In order to improve the visual perception of images of the reconstructed attenuation coefficient of the OCT signal and reduce noise outside the structural image of the biological tissue, a mask was superimposed on the μ_{OCT} images. To calculate the mask image, the intensity of each pixel from the ROI of the original OCT image was compared with a threshold value (the noise level of the OCT system). If the intensity was less than or equal to the threshold, the intensity of the corresponding mask pixel was assumed to be 0. If the pixel intensity was greater than the threshold value, the intensity of the mask's advisory pixel was assumed to be 1. To determine the threshold value, a rectangular area measuring approximately $250 \mu\text{m}$ in depth and $5000 \mu\text{m}$ in width outside the structural image of the biological tissue was selected on each OCT scan, from which the average and standard deviation of the pixel intensity were calculated. The threshold value was the sum of the mean and twice the standard deviation. To reduce the influence of speckle noise, an erosion filter with a window width of 3 pixels was used for the mask image. Thus, when an image mask was applied to the OCT signal attenuation coefficient image, the μ_{OCT} values, where the mask pixels were equal to 0, correspond to the zero values. In other cases, the μ_{OCT} values remained unchanged. Figure 2 shows a flowchart for calculating the average depth profile of the OCT signal attenuation coefficient for one B-scan.

Based on the calculated average depth profiles of the OCT signal attenuation coefficient, the average OCT signal attenuation coefficient was calculated at depths from 30 to $150 \mu\text{m}$ and from 350 to $550 \mu\text{m}$. The first averaging section is associated with the epidermis, the second section corresponds to the dermis region on the structural OCT image. Averaged μ_{OCT} coefficients for two depth intervals were calculated for each time point.

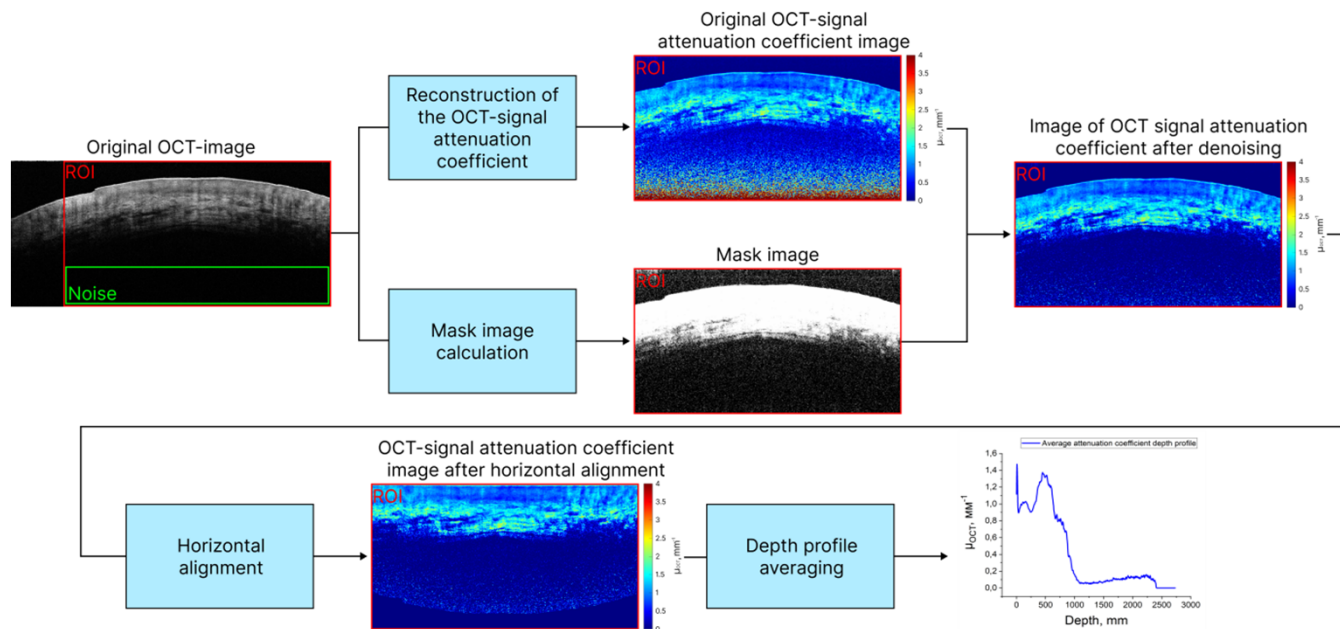


FIGURE 2 Block diagram of the algorithm for processing optical coherence tomography (OCT) data of the donor nail bed to calculate the average depth profile of the OCT signal attenuation coefficient.

2.3 | Laser aggregometry

The blood for laser aggregometry and laser diffractometry measurements was drawn from the cubital vein of one healthy male donor on an empty stomach in EDTA K3 tubes. The volunteer gave informed consent in accordance with the Declaration of Helsinki and the study was approved by the Ethics Committee of Medical Research and Educational Center of M.V. Lomonosov Moscow State University (protocol No. 6/23; October 16, 2023).

In order to measure the effect of glycerol on micro-rheological properties of RBC, the blood samples with glycerol concentration in 5%, 10%, 15%, 20% were prepared. All samples were prepared according to the following protocol. Freshly drawn blood was centrifuged for 10 min at 1600 rpm (170 g) at the room temperature ($T = 22^\circ\text{C}$). Then plasma was separated from the RBC mass. After that, glycerol 100% was added to the plasma and the sample was mixed. Then the RBC mass was added to the sample. Glycerol concentrations were selected in such a way that the final sample contained glycerol at the studied concentrations. Time of incubation was no longer than 1–2 min at the temperature 37°C . The control samples, that is, without OCA, were prepared by mixing the blood plasma with the aliquots of distilled water and addition of RBC mass in order to equalize the level of proteins in the samples. Also, the control sample without the addition of any OCA or water was prepared using blood plasma and blood mass. All samples had the same hematocrit ($\text{htc} = 45\%$).

Changes in microrheological properties of RBC caused by glycerol were measured by laser aggregometer and diffractometer of RBC RheoScan (RheoMeditech, Republic of Korea) [38, 39] allowing to measure the RBC microrheological properties using disposable cuvettes. To obtain information about such aggregation parameters of blood as the characteristic time of cell aggregation and aggregation index (AI) RheoScan cuvette of the first type was used (RSA-C01 chip). Cuvette has a metal stirring bar, that can be rotated by the magnetic field inside the device. The investigated blood sample in the volume ($8 \mu\text{L}$) was placed inside the thin ($500 \mu\text{m}$) cuvette chamber by micropipette.

The device registered the time dependence of the intensity of laser light ($\lambda = 633 \text{ nm}$) scattered forward by the blood sample. A typical aggregation kinetics is presented in Figure 3A. Right after the beginning of measurement, the stirring bar was rotated at high speed, dispersing all aggregates formed at stasis conditions inside the cuvette. During this process the registered scattered light intensity of laser decreased ($t < 0$). At $t = 0$, the bar rotation was stopped immediately. Then, the process of spontaneous aggregation of RBC at stasis (without applied shear stress) in the blood sample occurs. From light scattering theory, it is known that the larger the particle, that is, the larger the RBC aggregate, the more light is scattered in forward direction [40]. Thus, once spontaneous RBC aggregation begins, forward scattered light monotonically increases, as the size of the RBC aggregates monotonically increases.

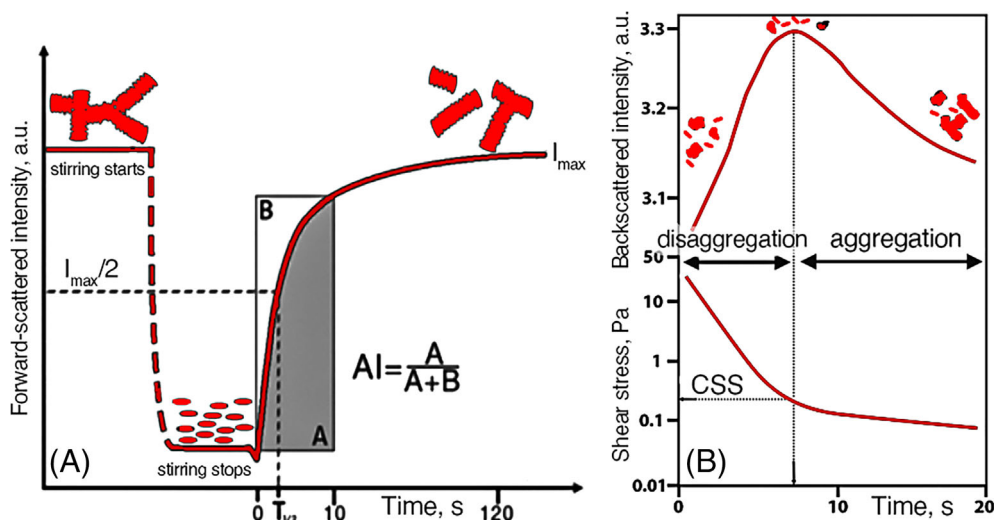


FIGURE 3 (A) Kinetics of RBC's spontaneous aggregation recorded by the RheoScan device. I_{\max} is the intensity of light scattered forward from the whole-blood layer when the aggregation of RBC is maximum; AI is the aggregation index; and $T_{1/2}$ is the characteristic time of aggregate formation. (B) Schematic diagrams of the critical shear stress (CSS) measurement process. CSS is a minimum shear stress that should be applied to the aggregated cells to start the process of their disaggregation.

The parameter $T_{1/2}$, which characterizes the time of aggregate formation was measured as the time during which the intensity of light scattered forward reaches half of the saturation intensity value at maximum aggregation after 120 s (Figure 3A). The parameter AI characterizes the number of RBCs aggregated during the first 10 s as a percentage. It is calculated as the ratio between the area under the aggregation curve and the whole area below and above the curve during the first 10 s of spontaneous aggregation process (Figure 3A).

To measure the critical shear stress (CSS) parameter the different type of RheoScan cuvette (RSD-K01 chip) with a microchannel (0.2 mm high \times 4.0 mm wide \times 40 mm long) with sample and waste chamber on the microchannel sides was used. Sample chamber was filled up with 0.5 mL of the sample. At the beginning of the experiment, a pressure difference (from 20 to 0 Pascals) was created in the microchannel, as a result of which the blood sample began to flow through the microchannel. The device registered the intensity of light back scattered from the flow. A schematic presentation of the process is shown in Figure 3B. During the first 10 s of the measurement due to the high shear stress inside the microchannel, the intensity of light scattered in the opposite backward direction increased as a result of the destruction of the aggregates formed earlier. However, when the shear stress in the microchannel reached the CSS point, it did not suffice to destroy the aggregates and the registered intensity started decreasing. As a result, the CSS is a minimum shear stress that should be applied to the aggregates to start the process of their disaggregation. This value characterizes the hydrodynamic strength of aggregates.

2.4 | Laser diffractometry

Laser diffractometry was used to obtain the shear-induced deformation parameters of RBCs implementing the RheoScan diffractometer (i.e., ektacytometry) [41, 42]. For these experiments, the same cuvette as for CSS measurements was used (RSD-K01 chip). To prepare the sample, the whole blood was diluted in 5.5% polyvinylpyrrolidone solution (htc = 1%) (viscosity 30 mPa \times s at 37°C).

The method is based on processing the diffraction pattern obtained on a screen located in the far field zone after diffraction of laser beam on a flow of a highly diluted suspension of RBCs under the influence of shear stress (from 20 to 0.5 Pa) [41, 42]. While the shear stress magnitude in the channel is low the RBCs have their normal round shape, without any deformation. In these conditions, the RBCs are oriented in such a way that their cross section resembles a circle. After shining onto this sample with a laser beam the iso-intensity lines of the produced diffraction pattern will, respectively, have the shape of a circle. Following an increase in the shear stress, the RBCs are pulled along the flow, taking on the shape of an ellipse. As a result, the iso-intensity lines of the obtained diffraction pattern also change their shape to elliptical because this pattern is formed as a superposition of diffraction patterns from many individual cells.

In order to obtain the information about the degree of ellipticity of the diffraction pattern it was approximated with an ellipse along an iso-intensity line. The resulting deformability of RBCs can be characterized by deformability index (DI) parameter, as a function of shear stress, which is calculated using the following equation [41]:

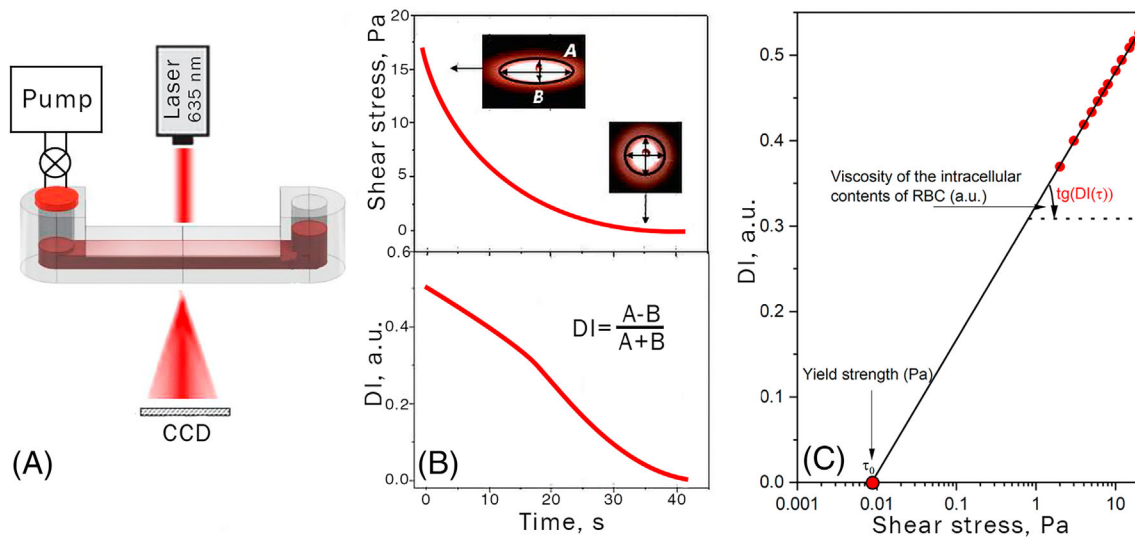


FIGURE 4 (A) Schematic representation of the principle of measuring DI on a RheoScan device; (B) time dependences of shear stress and DI calculated from corresponding diffraction patterns; (C) dependence of the RBC deformability index on the shear stress, represented in logarithm scale.

$$DI = \frac{A - B}{A + B}, \quad (4)$$

where A and B are the large and small axes of the ellipse respectively (Figure 4B).

Additionally, the obtained dependence of DI on shear stress was processed in order to reveal the information about yield strength of RBCs and viscosity of their intracellular contents. These parameters were described by Firsov et al. [43]. The relationship between DI and shear stress in semi-log scale was approximated using linear regression. The change in the viscosity of the intracellular contents of RBC can be estimated by the change in the slope of the plotted dependence of DI versus logarithm of shear stress, while the yield strength is determined by the value of shear stress corresponding to the intersection point of this curve with the X-axis (Figure 4C). Yield strength represents the minimum shear stress required for RBC deformation.

2.5 | Vital digital capillaroscopy

To visualize the capillaries of the nail bed, the capillaroscope Kapillarskan-1 (AET, Moscow, Russia) was used. The setup was equipped with a high-speed CCD-camera TM-6740GE (JAI, Japan) which had 1/3" monochrome progressive scan IT CCD sensor (200 fps and resolution 640×480 px). A LED-based illuminating system was used to illuminate the area under study.

After 3–5 min of rest, 1–2 drops of OCA were applied to the nail bed area of a healthy volunteer. The capillary

blood velocity was measured after the treatment with OCAs. This technique is described in more detail in [44, 45]. For these experiments, only cedar oil, oleic acid, glycerol, Visipaque-270[®] were used as OCAs.

2.6 | Statistical analysis

The data were processed, and figures were plotted using Origin 2022 software. In the results section, the figures displaying box plots of the measured parameters show the box spanning from the first quartile (Q1) to the third quartile (Q3), with a median line. The whiskers in the figures indicate the standard deviations, with the mean values in the middle. The statistical significance of the differences between groups of samples was determined using the Mann–Whitney U test using SciPy library in Python. Two samplings were considered significantly different if the p -value was less than 0.05 ($*p < 0.05$; $**p < 0.01$; $***p < 0.001$). The data in the tables are presented as the mean values \pm standard deviation.

3 | RESULTS AND DISCUSSION

3.1 | Evaluation of OCA efficiency with OCT

Figure 5 shows normalized diagrams for the initial value of the change in the attenuation coefficient when using various OCAs; the value of the attenuation coefficient of

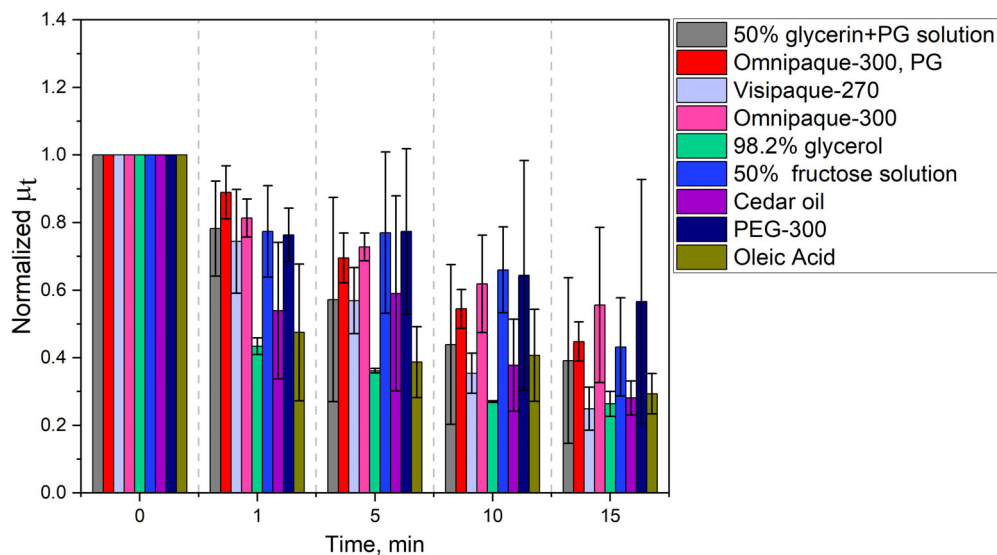


FIGURE 5 Dependence of the attenuation coefficient on time under application for various optical clearing agents. The whiskers are the standard deviations.

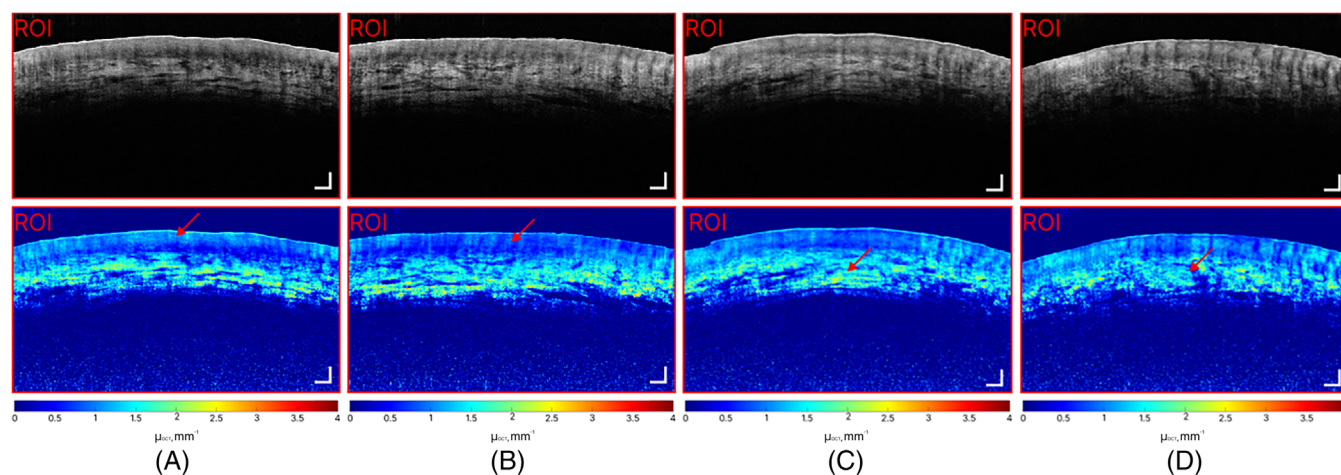


FIGURE 6 Typical optical coherence tomography (OCT) images in the region of interest of the nail bed skin and corresponding reconstructed OCT signal attenuation coefficient images before (A and C) and 15 min after application of oleic acid (B) and PEG-300 (D); the scale mark corresponds to 250 μm , red arrows indicate the epidermis (A and B) and dermis (C and D).

intact skin was considered at 0 min. The attenuation coefficient was calculated using Equation 1.

The obtained results demonstrate a decrease in the attenuation coefficient in comparison with intact skin when using various OCAs, which indicates the effectiveness of using these OCAs to reduce scattering from the skin during optical clearing. The use of 98.2% glycerol solution showed the most noticeable optical clearing effect: the attenuation coefficient decreased by 74% 15 min after application to the skin. Using Visipaque-270[®], the attenuation coefficient was reduced by 76%. The use of Cedar oil and oleic acid produced a reduction of the attenuation coefficient of the skin by 72% and 71%, respectively.

Figure 6 shows typical OCT images of the nail bed skin and the corresponding reconstructed OCT signal

attenuation coefficient images before and 15 min after application of oleic acid (Figure 6A,B) and PEG-300 (Figure 6C,D). It is easy to notice a decrease in the attenuation coefficient in the epidermal area after local application of the oleic acid for 15 min. At the same time PEG-300 causes a noticeable decrease in μ_{OCT} in the dermis.

Figure 7 shows typical images of the reconstructed OCT signal attenuation coefficient of the nail bed skin for different time points and OCAs. A pronounced effect of optical clearing of the epidermis and dermis is observed upon application of a 50% solution of glycerol and PG. When Visipaque-270[®] or a 50% solution of fructose are applied after 15 min, a decrease in the attenuation coefficient of the OCT signal in the dermis is observed, while the effect of PEG-300 or Omnipaque-300[®] is less pronounced. Differences in the attenuation coefficients of

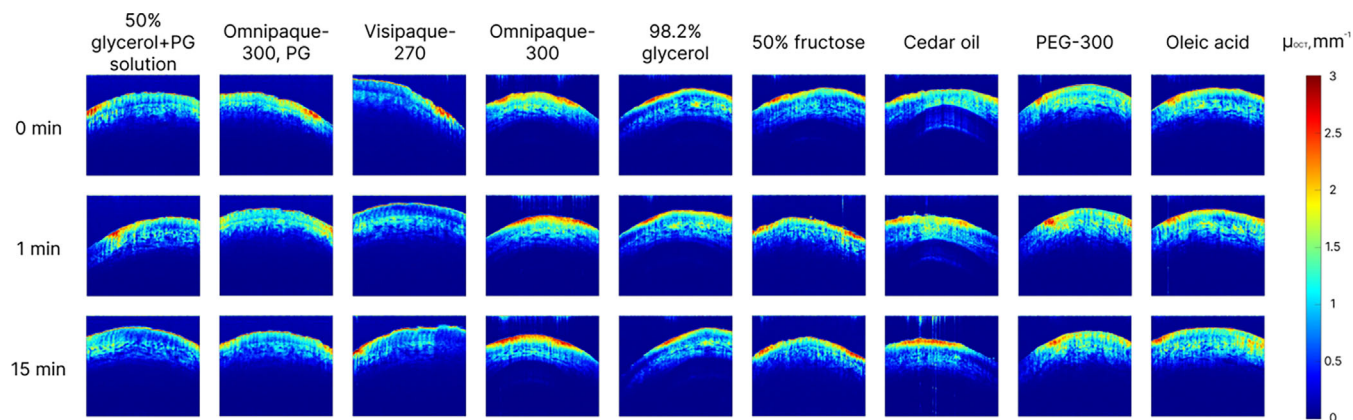


FIGURE 7 Typical images of the reconstructed attenuation coefficient of the optical coherence tomography signal of the nail bed skin for different time points and used optical clearing agents, the width and height of the image correspond to 6 and 2.7 mm, respectively.

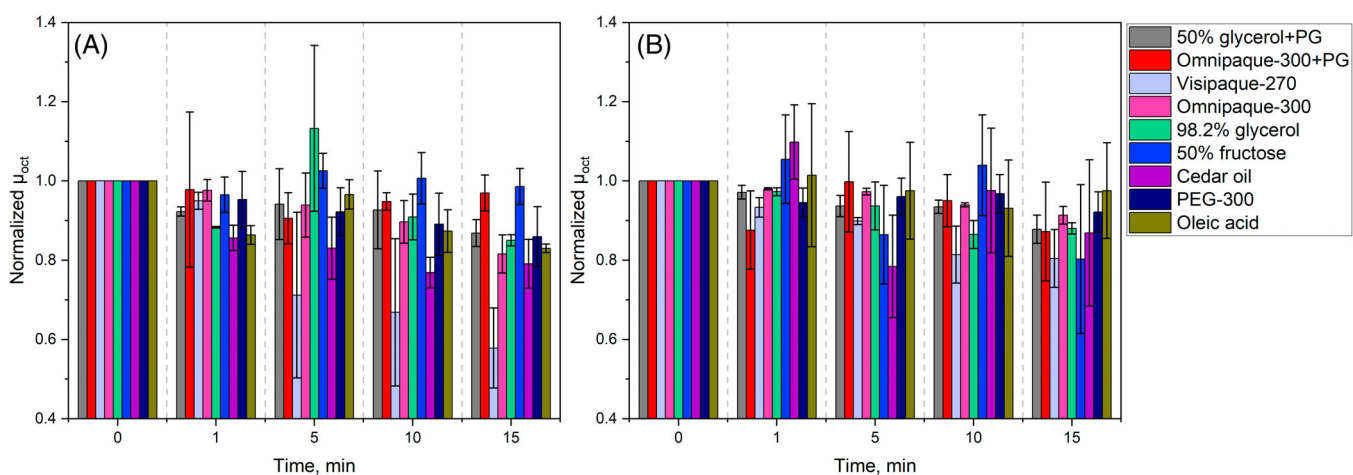


FIGURE 8 Dependences of the average μ_{OCT} coefficients at a depth of 30–150 μm , corresponding to the epidermis (A) and 350–550 μm corresponding to the dermis (B) on the time of exposure to various optical clearing agents. The whiskers are the standard deviations.

the OCT signal before the application of OCA may be due to the different state of intact skin both between the fingers of one volunteer and between volunteers.

Figure 8 shows the dependences of the average μ_{OCT} coefficients at a depth of 30–150 μm (epidermis) (Figure 8A) and 350–550 μm (dermis) (Figure 8B) on the time of exposure to various OCAs. It is easy to notice that the greatest effect of OC of the epidermis is observed with Visipaque-270[®], while a 50% solution of fructose or Omnipaque-300[®] did not show a noticeable effect within 15 min of application. However, a solution of fructose and glycerol leads to a decrease in the attenuation coefficient μ_{OCT} in the dermis, which may be due to the pronounced osmoticity of these OCAs and the induction of diffusion of free water from the deeper layers to the upper ones, which in turn is consistent with the data of the work [46].

In Figure 8A, the apparent increase in the attenuation coefficient was observed for the glycerol solution after 5 min of the treatment. Interestingly, this increment is observed only for the epidermis. It is known that high

concentration of glycerol leads to tissue dehydration, and it is possible that water from the dermis is extracted by glycerol into the epidermis in a short period of time, leading to an increase in the attenuation coefficient in the epidermis area [47].

3.2 | In vitro effect of OCAs on the microrheological properties of RBC

3.2.1 | Changes in RBC aggregation parameters: Results obtained using laser aggregometry

It is fair point to remind that the results in this section were obtained in vitro using OCA suspended in fresh human blood. We performed a preliminary study (not shown) and found that the blood aggregation and deformation properties were independent of the incubation time after OCA suspension. It seems that osmotic

changes and changes in RBC membrane properties are the main pathway of OCA influence on aggregation and deformation properties of blood.

Results in Figure 9 show that the CSS parameter increases statistically significantly for the glycerol concentrations of 10% and 20%.

Figure 10 shows that the AI parameter decreases with the increasing of glycerol concentration. Marked effect of glycerol can be observed for the concentrations 15% and 20%. AI decreases by $48 \pm 14\%$ for 15% glycerol solution, while in samples with distilled water the decrease is only $18 \pm 8\%$ for equal concentrations. For 20% glycerol solution, the decrease is $68 \pm 10\%$ and for water $36 \pm 8\%$. The decrease for glycerol solution is more significant, which means that for such concentration the changes are caused precisely by the influence of glycerol. We suppose that the reduction is caused by the decrease of DI for the samples with glycerol.

Figure 11 shows the dependence of the $T_{1/2}$ parameter on the concentration of the glycerol and amount of distilled water in the sample. The parameter increases with an increase in concentration of glycerol. Here, the effect of glycerol can be also observed for 15% and 20% concentrations. For samples with distilled water, the increase of $T_{1/2}$ is $38 \pm 26\%$ for 15% amount of water (9 s) and $134 \pm 60\%$ for 20% amount of water (15 s) in comparison with control sample (6 s). Samples with glycerol show bigger magnification. That justify the effect of glycerol. For samples with 15% and 20% concentrations, it is $132 \pm 45\%$ (14 s) and $318 \pm 134\%$ respectively (26 s).

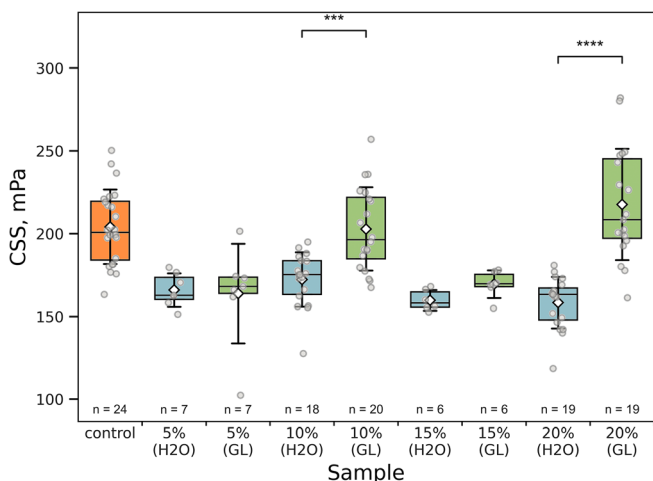


FIGURE 9 Dependence of the critical shear stress parameter on the concentration of glycerol and amount of distilled water in the sample. Control sample represents the blood with adjusted hematocrit without the addition of any optical clearing agent or water. Significant differences are presented only between glycerol and water samples with the same concentration. *** $p < 0.001$; **** $p < 0.0001$.

3.2.2 | Changes in RBC deformability: Results obtained using laser diffractometry

DI decreases with increasing glycerol concentration starting from 5% (Figure 12). For 5% solution it is $8 \pm 3\%$, for 10% it is $30 \pm 8\%$. There are no changes in samples with distilled water, that is why the marked effect of glycerol is observed here. During the incubation of RBCs with

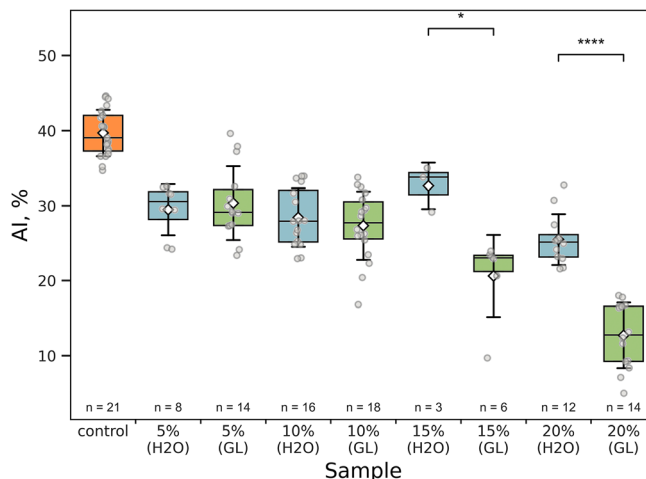


FIGURE 10 Dependence of the aggregation index parameter on the concentration of glycerol and amount of distilled water in the sample. Control sample represents the blood with adjusted hematocrit without the addition of any optical clearing agent or water. Significant differences are presented only between glycerol and water samples with the same concentration. * $p < 0.05$; **** $p < 0.0001$.

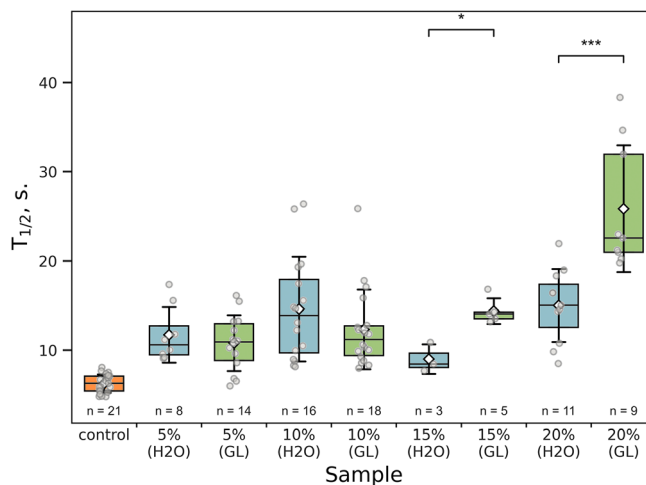


FIGURE 11 Dependence of the $T_{1/2}$ parameter on the concentration of the glycerol and amount of distilled water in the sample. Control sample represents the blood with adjusted hematocrit without the addition of any optical clearing agent or water. Significant differences are presented only between glycerol and water samples with the same concentration. * $p < 0.05$; *** $p < 0.001$.

glycerol, it penetrates inside the RBC through the membrane [48] and causes an increase in the viscosity of the intracellular contents (Figure 13). This may be the reason for the decrease in deformability. The yield strength decreases when increasing glycerol concentration (Figure 14). This means that glycerol not only penetrates the RBC membrane but also changes its properties.

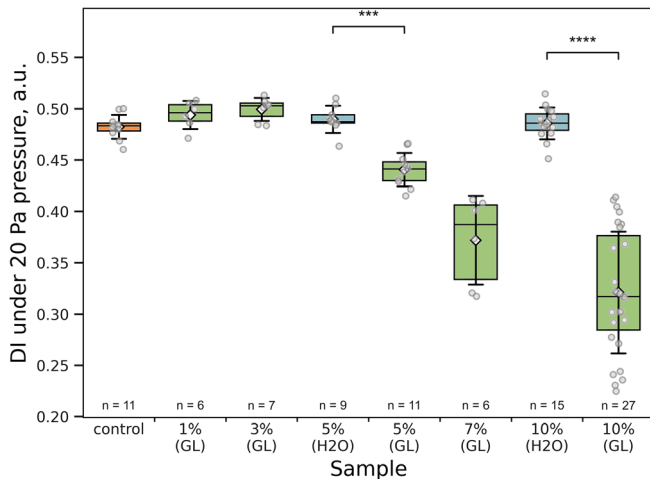


FIGURE 12 Dependence of the DI of RBC under 20 Pa on the concentration of the glycerol and amount of distilled water in the sample. Control sample represents the blood with adjusted hematocrit without the addition of any optical clearing agent or water. Significant differences are presented only between glycerol and water samples with the same concentration. *** $p < 0.001$; **** $p < 0.0001$.

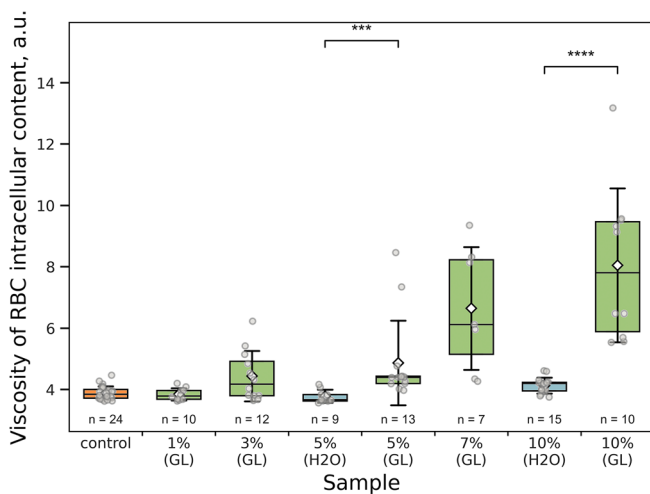


FIGURE 13 Dependence of the viscosity of the intracellular contents of RBC on the concentration of the glycerol and amount of distilled water in the sample. Control sample represents the blood with adjusted hematocrit without the addition of any optical clearing agent or water. Significant differences are presented only between glycerol and water samples with the same concentration. *** $p < 0.001$; **** $p < 0.0001$.

In this section, glycerol was shown to reduce the deformability and decrease the aggregation of RBC, which is consistent with the general results that the lower the deformability, the lower the aggregation of RBC [49].

3.3 | Effects of optical clearing agents assessed in vivo using nailfold digital capillaroscopy

The capillaroscopy method always involves the application of OCA to the finger being examined, since it is not possible to visualize the capillaries of the nail bed without any OCA. The typical images of single capillaries obtained using the vital digital capillaroscopy and four examined OCA after 5 min of application are presented in Figure 15. One can see that apart from Visipaque-270[®], other OCAs show somewhat similar contrast and image quality of the capillaries. The obtained results of capillary blood velocity depending on the clarifying OCA for capillaries of one healthy donor are shown in Figure 16. Capillary blood velocity depends on the OCA used, with statistically significant differences observed between Oleic acid and the following OCAs: Visipaque-270[®], 98.2% glycerol, and Cedar oil. The mechanism for the observed differences in the capillary blood flow velocity is most likely that OCA penetrates the skin and alters the properties of capillaries and blood cells.

Blood flow in large vessels and capillaries is different. By monitoring and analyzing the changes in the microcirculation parameters of blood in capillaries, clinicians can obtain

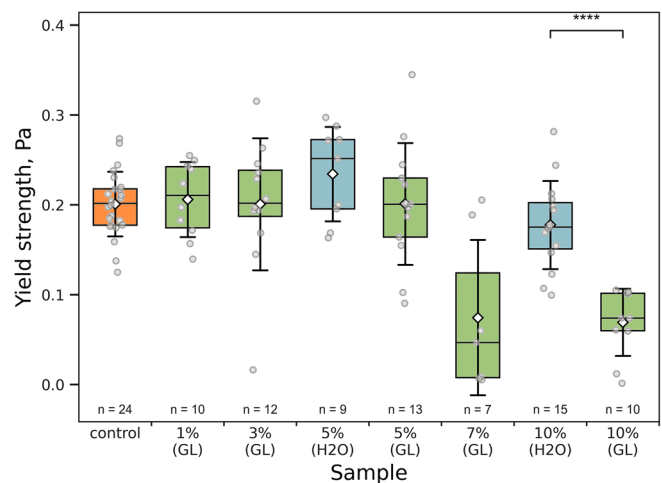


FIGURE 14 Dependence of the yield strength of RBC on the concentration of the glycerol and amount of distilled water in the sample. Control sample represents the blood with adjusted hematocrit without the addition of any optical clearing agent or water. Significant differences are presented only between glycerol and water samples with the same concentration. **** $p < 0.0001$.

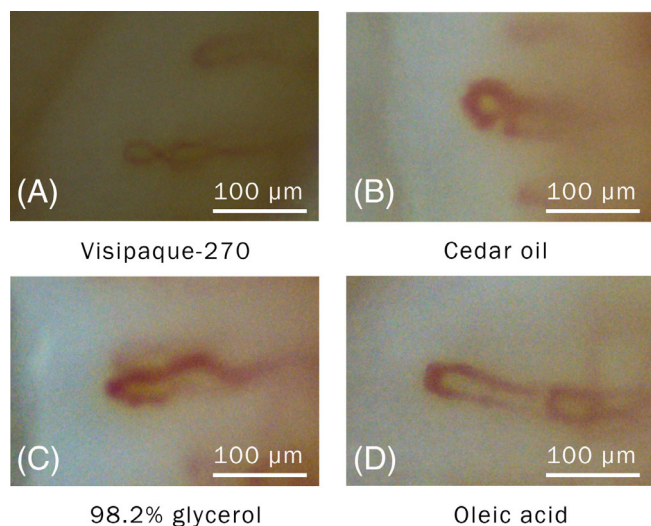


FIGURE 15 The typical images of single nail bed capillaries obtained using the vital digital capillaroscopy and (A) Visipaque-270[®], (B) Cedar oil, (C) 98.2% glycerol, and (D) Oleic acid as an OCA. The images were recorded 5 min after the OCA application. Magnification 400 \times .

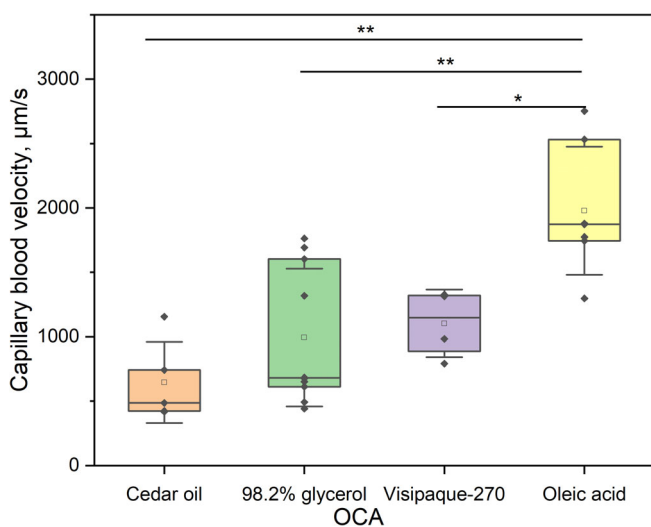


FIGURE 16 Dependence of the nail bed capillary blood velocity on the applied OCA agent. * $p < 0.05$; ** $p < 0.01$.

valuable information regarding individual reaction on treatment and control individual medical therapy [44].

4 | CONCLUSIONS

Preliminary findings suggest that the use of OCAs in our study significantly raises the transparency and enhances the visualization of the nail bed. These OCAs effectively reduce scattering and improve refraction during the imaging procedures, resulting in clearer images and improved access to deeper layers of the nail bed. Notably, glycerol

demonstrates the highest potential in reducing the attenuation coefficient compared to other OCAs. By refining optical clearing techniques, we believe that this research has the potential to enhance various techniques that visualize capillaries and evaluate blood perfusion. In vitro experiments have shown that glycerol reduces RBC aggregation and RBC deformation, and increases intracellular viscosity. We hypothesize that this change in deformability is due to the penetration of glycerol molecules into the RBC through the membrane, leading to its decreased deformability and aggregation. Also, in our study we demonstrated for the first time that application of OCA along with the benefits of optical clearing, leads to additional perturbations in the results of capillary blood flow velocity measurements due to changing the microrheological properties of RBC. This fact must be taken into account when conducting the measurements using digital capillaroscopy.

ACKNOWLEDGMENTS

All experiments, blood supply and data analysis were supported by the Russian Science Foundation Grant No. 23-45-00027. Evaluating the attenuation coefficient of the OCT signal in the epidermis and dermis by Surkov Yu. I. and Tuchin V. V. was conducted in the framework of the state assignment by the Ministry of Science and Higher Education of Russian Federation (project no. FSRR-2023-0007).

CONFLICT OF INTEREST STATEMENT

The authors declare no financial or commercial conflict of interest.

DATA AVAILABILITY STATEMENT

The data that support the findings of this study are available on request from the corresponding author. The data are not publicly available due to privacy or ethical restrictions.

ORCID

P. B. Ermolinskiy <https://orcid.org/0000-0002-4688-2307>

A. E. Lugovtsov <https://orcid.org/0000-0001-5222-8267>

P. A. Timoshina <https://orcid.org/0000-0003-4856-9522>

Y. I. Gurfinkel <https://orcid.org/0000-0002-1882-4329>

V. V. Tuchin <https://orcid.org/0000-0001-7479-2694>

A. V. Priezzhev <https://orcid.org/0000-0003-4216-7653>

REFERENCES

- [1] L. M. C. Oliveira, V. V. Tuchin, *The Optical Clearing Method*, Springer International Publishing, Cham, Switzerland **2019**.
- [2] Z. Wei, Q. Lin, E. N. Lazareva, P. A. Dyachenko(Timoshina), J. Yang, Y. Duan, V. V. Tuchin, *Laser Phys. Lett.* **2021**, *18*, 085603.
- [3] D. K. Tuchina, I. G. Meerovich, O. A. Sindeeva, V. V. Zherdeva, A. P. Savitsky, A. A. Bogdanov, V. V. Tuchin, *J. Biophotonics* **2020**, *13*, e201960249.

- [4] O. Hamdy, R. M. Abdelazeem, *J. Public Health Int.* **2020**, *2*, 13.
- [5] V. V. Tuchin, D. Zhu, E. A. Genina, *Handbook of Tissue Optical Clearing*, CRC Press, Boca Raton, FL **2021**.
- [6] P. A. Dyachenko (Timoshina), A. S. Abdurashitov, O. V. Semyachkina-Glushkovskaya, V. V. Tuchin, *Handbook of Tissue Optical Clearing*, CRC Press, Boca Raton, FL **2021**, p. 393.
- [7] J. Zhu, D. Li, T. Yu, D. Zhu, *J. Innov. Opt. Health Sci.* **2022**, *15*, 2230002.
- [8] O. S. Zhernovaya, E. A. Genina, V. V. Tuchin, A. N. Bashkatov, *Handbook of Tissue Optical Clearing*, CRC Press, Boca Raton, FL **2021**, p. 383.
- [9] J. Cvjetinovic, D. V. Nozdriukhin, M. Mokrousov, A. Novikov, M. V. Novoselova, V. V. Tuchin, D. A. Gorin, *Handbook of Tissue Optical Clearing*, CRC Press, Boca Raton, FL **2021**, p. 419.
- [10] P. A. Dyachenko, L. E. Dolotov, E. N. Lazareva, A. A. Kozlova, O. A. Inozemtseva, R. A. Verkhovskii, G. A. Afanaseva, N. A. Shushunova, V. V. Tuchin, E. I. Galanzha, V. P. Zharov, *IEEE J. Sel. Top. Quantum Electron.* **2021**, *27*, 1.
- [11] I. Y. Yanina, Y. Tanikawa, E. A. Genina, P. A. Dyachenko, D. K. Tuchina, A. N. Bashkatov, L. E. Dolotov, Y. V. Tarakanchikova, G. S. Terentuk, N. A. Navolokin, A. B. Bucharskaya, G. N. Maslyakova, Y. Iga, S. Takimoto, V. V. Tuchin, *J. Biophotonics* **2022**, *15*, e202100393.
- [12] C. Zhang, W. Feng, *Lasers Surg. Med.* **2022**, *54*, 447.
- [13] G. R. Musina, A. A. Gavidush, N. V. Chernomyrdin, I. N. Dolganova, V. E. Ulitko, O. P. Cherkasova, V. N. Kurlov, G. A. Komandin, I. V. Zhivotovskii, V. V. Tuchin, K. I. Zaytsev, *Opt. Spectrosc.* **2020**, *128*, 1026.
- [14] D. K. Tuchina, A. B. Bucharskaya, P. A. Dyachenko (Timoshina), N. I. Dikht, G. S. Terentyuk, V. V. Tuchin, *Biomedical Photonics for Diabetes Research*, CRC Press, Boca Raton, FL **2022**, p. 1.
- [15] D. K. Tuchina, V. V. Tuchin, *Handbook of Tissue Optical Clearing*, CRC Press, Boca Raton, FL **2021**, p. 517.
- [16] T. Yu, J. Zhu, D. Li, D. Zhu, *iScience* **2021**, *24*, 102178.
- [17] O. Baskurt, B. Neu, H. J. Meiselman, *Red Blood Cell Aggregation*, CRC Press, Boca Raton, FL **2011**.
- [18] S. M. Zaytsev, M. Amouroux, V. V. Tuchin, E. A. Genina, W. Blondel, *J. Biomed. Opt.* **2023**, *28*, 055002.
- [19] S. M. Zaytsev, Y. I. Svenskaya, E. V. Lengert, G. S. Terentyuk, A. N. Bashkatov, V. V. Tuchin, E. A. Genina, *J. Biophotonics* **2020**, *13*, e201960020.
- [20] M. Varaka, M. Z. Vardaki, G. Gaitanis, I. D. Bassukas, N. Kourkoumelis, *Appl. Sci.* **2022**, *12*, 8277.
- [21] A. Y. Sdobnov, J. Lademann, M. E. Darwin, V. V. Tuchin, *Biochemistry (Moscow)* **2019**, *84*, 144.
- [22] I. T. Shagautdinova, A. M. Likhter, K. V. Berezin, K. N. Dvoretzky, V. V. Nechaev, V. V. Tuchin, *J. Phys. Conf. Ser.* **2021**, *2103*, 012048.
- [23] K. V. Berezin, K. N. Dvoretzky, M. L. Chernavina, V. V. Nechaev, A. M. Likhter, I. T. Shagautdinova, E. M. Antonova, V. V. Tuchin, *J. Phys. Conf. Ser.* **2019**, *1400*, 033018.
- [24] K. N. Dvoretzky, K. V. Berezin, M. L. Chernavina, A. M. Likhter, I. T. Shagautdinova, E. M. Antonova, O. N. Grechukhina, V. V. Tuchin, *J. Surf. Invest.: X-Ray, Synchrotron Neutron Tech.* **2018**, *12*, 961.
- [25] K. V. Berezin, K. N. Dvoretzky, V. V. Nechaev, A. M. Likhter, I. T. Shagautdinova, V. V. Tuchin, *J. Biomed. Photonics Eng.* **2020**, *6*, 020308.
- [26] A. N. Bashkatov, K. V. Berezin, K. N. Dvoretzky, M. L. Chernavina, E. A. Genina, V. D. Genin, V. I. Kochubey, *J. Biomed. Opt.* **2018**, *23*, 1.
- [27] M. V. Gómez-Gaviro, D. Sanderson, J. Ripoll, M. Desco, *iScience* **2020**, *23*, 101432.
- [28] The structure of propylene glycol, <https://pubchem.ncbi.nlm.nih.gov/compound/Propylene-Glycol>.
- [29] The structure of Omnipaque-300[®], <https://dailymed.nlm.nih.gov/dailymed/fda/fdaDrugXsl.cfm?setid=442aed6e-6242-4a96-90aa-d988b62d55e8>.
- [30] The structure of cedar oil, <https://www.guideschem.com/encyclopedia/cedar-leaf-oil-dic355497.html>.
- [31] The structure of Visipaque-270[®], <https://pubchem.ncbi.nlm.nih.gov/compound/Iodixanol>.
- [32] The structure of oleic acid, <https://pubchem.ncbi.nlm.nih.gov/compound/Oleic-Acid>.
- [33] I. Costantini, R. Cicchi, L. Silvestri, F. Vanzi, F. S. Pavone, *Biomed. Opt. Express* **2019**, *10*, 5251.
- [34] E. A. Genina, A. N. Bashkatov, E. A. Kolesnikova, M. V. Basko, G. S. Terentyuk, V. V. Tuchin, *J. Biomed. Opt.* **2013**, *19*, 021109.
- [35] K. A. Vermeer, J. Mo, J. J. A. Weda, H. G. Lemij, J. F. de Boer, *Biomed. Opt. Express* **2014**, *5*, 322.
- [36] B. Karamata, P. Lambelet, M. Laubscher, M. Leutenegger, S. Bourquin, T. Lasser, *J. Opt. Soc. Am. A* **2005**, *22*, 1369.
- [37] P. Lee, W. Gao, X. Zhang, *Appl. Opt.* **2010**, *49*, 3538.
- [38] S. Shin, Y. Yang, J.-S. Suh, *Clin. Hemorheol. Microcirc.* **2009**, *41*, 197.
- [39] A. N. Semenov, A. E. Lugovtsov, E. A. Shirshin, B. P. Yakimov, P. B. Ermolinskiy, P. Y. Bikhmulina, D. S. Kudryavtsev, P. S. Timashev, A. V. Muravyov, C. Wagner, S. Shin, A. V. Priezzhev, *Biomolecules* **2020**, *10*, 1448.
- [40] S. V. Tsinopoulos, E. J. Sellountos, D. Polyzos, *Appl. Opt.* **2002**, *41*, 1408.
- [41] S. Shin, J. X. Hou, J. S. Suh, M. Singh, *Clin. Hemorheol. Microcirc.* **2007**, *37*, 319.
- [42] H. Lee, W. Na, S. B. Lee, C. W. Ahn, J. S. Moon, K. C. Won, S. Shin, *Front. Physiol.* **2019**, *10*, 1062.
- [43] N. N. Firsov, A. V. Priezzhev, N. V. Klimova, A. Y. Tyurina, *J. Eng. Phys. Thermophys.* **2006**, *79*, 118.
- [44] P. Ermolinskiy, Y. Gurfinkel, E. Sovetnikov, A. Lugovtsov, A. Priezzhev, *Life* **2023**, *13*, 2043.
- [45] Y. I. Gurfinkel, M. L. Sasonko, M. I. Kuznetsov, A. V. Priezzhev, *2015 International Conference on BioPhotonics (BioPhotonics)*, IEEE, Florence, Italy **2015**, p. 1.
- [46] A. Y. Sdobnov, M. E. Darwin, J. Schleusener, J. Lademann, V. V. Tuchin, *J. Biophotonics* **2019**, *12*, e201800283.
- [47] C.-K. Lee, M.-T. Tsai, F.-Y. Chang, C.-H. Yang, S.-C. Shen, O. Yuan, C.-H. Yang, *Sensors* **2013**, *13*, 4041.
- [48] C. R. Valeri, G. Ragno, *Transfus. Apher. Sci.* **2006**, *34*, 271.
- [49] A. I. Maslianitsyna, P. B. Ermolinsky, A. E. Lugovtsov, A. V. Priezzhev, *J. Biomed. Photonics Eng.* **2020**, *6*, 020305.

How to cite this article: P. A. Moldon, P. B. Ermolinskiy, A. E. Lugovtsov, P. A. Timoshina, E. N. Lazareva, Y. I. Surkov, Y. I. Gurfinkel, V. V. Tuchin, A. V. Priezzhev, *J. Biophotonics* **2024**, e202300524. <https://doi.org/10.1002/jbio.202300524>